Facet-Level Mechanistic Insights into General Homogeneous Carbon Doping for Enhanced Solar-to-Hydrogen Conversion

*Jie Li, Kun Zhao, Ying Yu, and Lizhi Zhang**

Homogeneous doping can boost solar-to-hydrogen conversion and therefore attracts great attention. Although a great deal of effort has been made to explore the doping–photoreactivity relationship, the doping mechanisms, especially from the perspective of crystal facets, are seldom explored. In this study, a general homogeneous carbon doping strategy is established and then serves as the doping model for a mechanistic investigation, as encouraged by its versatility in enabling homogeneous incorporation of carbon and improving solar-to-hydrogen conversion for typical oxides including TiO_2, ZnO, and BiOCl. Using well-defined BiOCl nanosheets of high {001} or {010} facet exposure, we clarify the homogeneous carbon doping mechanism at the level of crystal facets for the first time. This mechanism involves the initial facet-dependent adsorption of the dopant precursor, regulated by the surface atomic structures, and the subsequent facet-dependent diffusion of carbon dopants associated with the facet-related arrangements of bulk atoms. This results in facet-dependent carbon doping behavior and a dopant-concentration-dependent solar-to-hydrogen conversion property of BiOCl nanosheets. These mechanistic insights also suggest that the implantation of the dopant precursor in the shallow lattice of host nanocrystal is vital for the effective homogeneous doping. This new doping model is different from the conventional counterpart based on the organic ligands or gas molecules adsorption onto the surface of host nanocrystals, where surface doping usually occurs.

1. Introduction

Doping chemistry is of fundamental and technological significance in the field of materials, especially for advancing nanotechnology development to solve the forthcoming energy crisis in the future, because doping mediated modifications of band structure endow nanomaterials with dramatically improved functionality that converts renewable solar energy into clean hydrogen fuel, a next-generation high-density energy carrier.[1] In most doping cases, surface doping usually occurred, extending optical absorption range but triggering the formation of bulk lattice defects as the recombination centers of photogenerated carriers to decrease nanomaterial photoactivity.[2] Whereas homogeneous doping, though emerging in few cases, enabled the uniform and ordered distribution of dopant within the frameworks of host nanocrystals, which could improve both light absorption and charge transport.[3] The motivation of achieving highly efficient solar-to-hydrogen conversion inspired the immense research interests on homogeneous doping, thereby prompting the emergence of various homogeneous doping strategies, such as heteroatom incorporation into oxides (N-doped TiO_2, $Cs_{0.68}Ti_{1.83}O_4$, and HNb_3O_8; transition-metal-doped TiO_2), atom and molecule substitution in nitrides (S- and B-doped and thiophene-incorporated C_3N_4), and design of solid–solution structures ($(Ga_{1-x}Zn_x)(N_{1-x}O_x)$, $Zn_xCd_{1-x}S$, $AgAl_{1-x}Ga_xO_2$).[4] These doping strategies required the initial adsorption of dopant precursor of either organic ligands or gas molecules on the host crystal surface and their subsequent incorporation from the exterior to the interior of host crystal. These two processes occurred at host-crystal/dopant-precursor interfaces (solid/liquid, solid/gas, solid/solid).[5] The nature of this interfacial reaction strongly correlates the doping process with the surface properties of host crystals, especially the surface atomic structures regulated by the facet exposure. However, the detailed roles of crystal facet in doping are seldom explored, although many efforts have been made to enhance the photoreactivity with homogeneous doping, and Erwin et al. theoretically mentioned the importance of crystal facet for doping.[6] Therefore, unraveling the correlation of crystal facet with doping steps is urgent and also vital for the high-performance doped photocatalyst design, but still challenging.

J. Li, K. Zhao, Prof. L. Zhang
Key Laboratory of Pesticide & Chemical Biology of Ministry of Education
Institute of Environmental Chemistry
College of Chemistry
Central China Normal University
Wuhan 430079, P.R. China
E-mail: zhanglz@mail.ccnu.edu.cn
J. Li, Prof. Y. Yu
Institute of Nanoscience and Nanotechnology
College of Physical Science and Technology
Central China Normal University
Wuhan 430079, P.R. China

DOI: 10.1002/adfm.201404178

The realization of this goal relies on the development of a general homogeneous doping strategy, which is never reported to the best of our knowledge. Among various doping strategies, carbon doping has been reported theoretically and experimentally to be highly efficient for the photoactivity improvement, but its mechanistic investigation has not been performed.[1a,d,2b,7] Herein, we develop a general homogeneous carbon doping strategy comprised of initial bottom-up hydrothermal processing and subsequent thermal treatment. Its universality is identified by its applicability to enable homogeneous incorporation of carbon and improve solar-to-hydrogen conversion for typical oxides including TiO_2, ZnO, and BiOCl. The universality of this homogeneous carbon doping encourages us to further clarify the underlying mechanism, especially at a crystal facet level.

Facet-level mechanistic insight into the doping process requires the use of model materials with high percentage of facet exposure to eliminate the effect of coexisting facets as much as possible. Despite of tremendous efforts on the crystal facet engineering of TiO_2 and ZnO, their facet exposure percentages were rarely up to 80%. Moreover, their two sets of samples with different facet exposure could not be fabricated with similar reaction conditions (e.g., temperature) and reactant precursors simultaneously.[8] Our recent facet-controllable synthesis of BiOCl offered a solution to obtain two sets of nanosheets with high facet exposure percentages under the same hydrothermal reaction temperature and the similar reactant precursors.[9] With the utilization of a general homogeneous carbon doping strategy on the BiOCl nanosheets of high {001} or {010} facet exposure, we therefore attempt to experimentally clarify the homogeneous carbon doping mechanism at a crystal facet level for the first time. The intrinsic roles of the pre-adsorption of dopant precursor in the shallow lattice of host nanocrystal during the effective homogeneous doping process are investigated in detail.

2. Results and Discussion

2.1. Homogeneous Carbon Doping Process

Homogeneous carbon doping strategy was realized via an initial bottom-up hydrothermal processing and a subsequent thermal treatment with glucose as the carbon dopant source (**Figure 1**). Typically, a hydrothermal-induced glucose carbonization route was first applied for the pre-adsorption of carbon dopant precursor in the form of carbonaceous species. Next, thermal treatment in air was performed to trigger the diffusion of carbon dopant toward the effective substitution of host lattice atom, leading to the formation of homogeneous carbon doping. In this study, the three most commonly investigated photocatalysts, TiO_2, ZnO, and BiOCl, were used to demonstrate this homogeneous carbon doping strategy. The crystallographic structure and phase purity of the as-prepared carbon doped samples were examined by x-ray diffraction (XRD) analysis. The diffraction peaks of TiO_2-HC, ZnO-HC, BOC-001HC, and BOC-010HC (Figure S1, Supporting Information) could be unambiguously indexed to TiO_2, ZnO, and BiOCl phases, respectively, and no impurity peaks were detected in the XRD patterns, revealing the reliability and the feasibility of this carbon doping strategy without causing the phase transition of host nanocrystals. Our previous synthetic methodology could also realize the facet-controllable exposure of carbon doped BiOCl via adjusting the pH value of precursor solution. As revealed by high-resolution transmission electron microscopy (HRTEM) images (Figures S2 and S3, Supporting Information), only irregular nanoparticles were observed for carbon doped TiO_2 and ZnO, whereas the {001}- and {010}-faceted BiOCl obtained at pH levels of 1 and 6 possessed well-defined nanosheet configuration with facet exposure percentages of as high as 93% and 91%, respectively.

2.2. Characterization of Homogeneous Carbon Doping

Time-dependent x-ray photoelectron spectroscopy (XPS) analysis (also the XPS depth profiling technique) was first used to check the homogeneous carbon doping in the TiO_2, ZnO, and BiOCl. Besides the C 1s peak at 284.6 eV arising from the adventitious carbon, a new peak signal appeared at 282.6 eV. The signal intensity of this new peak kept unchanged upon Ar^+ sputtering from 0 to 1200 s (**Figure 2**), while the peak of adventitious carbon disappeared completely only after 240 s Ar^+ sputtering. This phenomenon strongly suggested the incorporation of carbon dopants into their lattices to form C—Ti, C—Zn, and C—Bi bonds, consistent with the reported results,[7c,d,10] and also indicated the homogeneous distribution of carbon dopants within the framework of host lattices. The relative atomic concentrations can be estimated by normalizing XPS peak area with atomic sensitivity factor according to the following equation

$$n_1 / n_2 = (I_1 / S_1) / (I_2 / S_2) \quad (1)$$

where n_1 and n_2 represent the atomic numbers of element 1 and 2, I_1 and I_2 are the XPS peak area, and S_1 and S_2 are the sensitivity factors.[4b,f] The calculated atomic concentrations were 0.41%, 0.36%, 0.51%, and 2.98%, for C-doped TiO_2, ZnO, and BiOCl with exposed {001} or {010} facet, respectively. Compared to TiO_2 and ZnO, BiOCl was homogeneously incorporated with more carbon dopants. More interestingly, much higher contents of carbon dopants was found

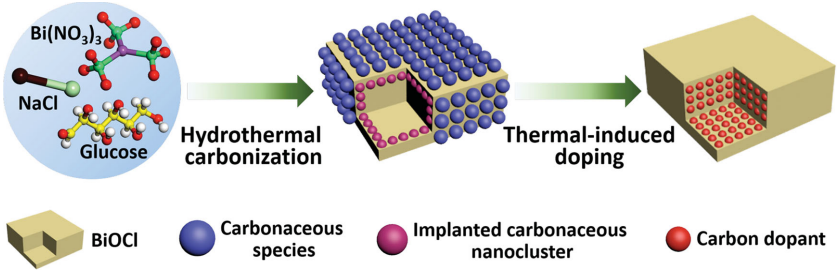

Figure 1. Schematic illustration of homogeneous carbon doping strategy comprised of bottom-up hydrothermal processing and subsequent thermal treatment with taking carbon doped BiOCl as the example.

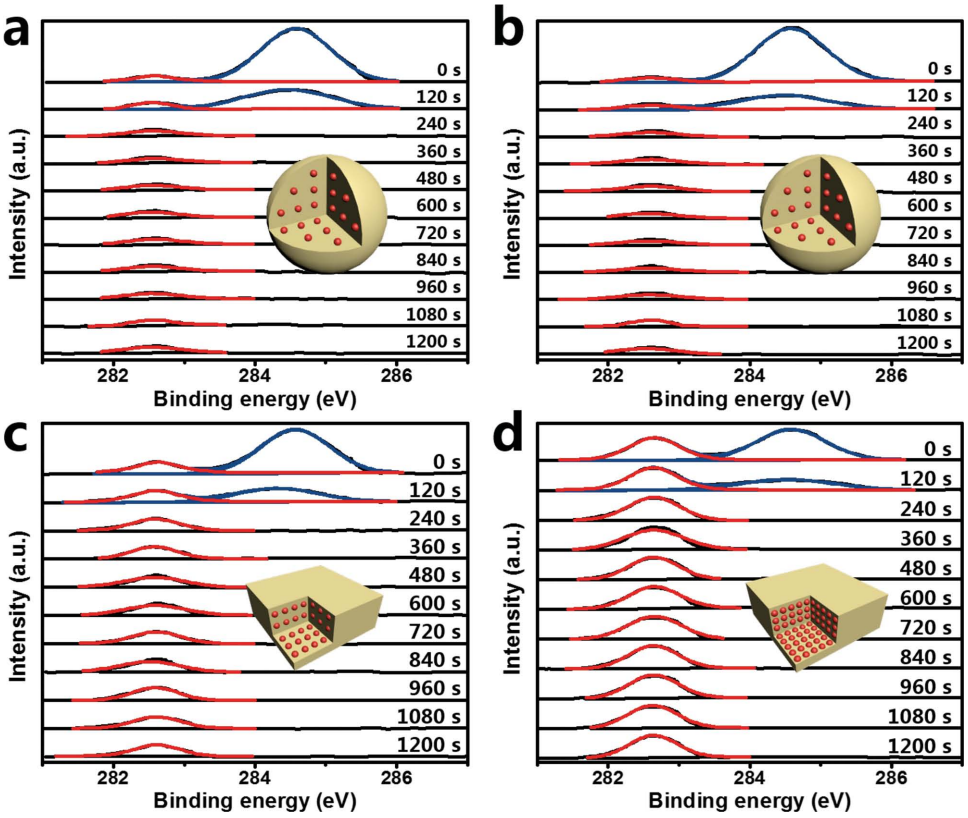

Figure 2. Time-dependent high resolution C 1s XPS spectra of TiO_2-HC a), ZnO-HC b), BOC-001HC c), and BOC-010HC d) upon Ar^+ sputtering demonstrating the homogeneity of carbon dopant in their frameworks.

in BiOCl with exposed {010} facet relative to the {001} counterparts, suggesting the facet dependent carbon doping behavior of BiOCl.

UV–visible absorption spectra were further utilized to probe the homogeneous carbon doping in the TiO_2, ZnO, and BiOCl. Homogeneous carbon doping endowed TiO_2, ZnO, and BiOCl with the overall red-shift of the intrinsic absorption edge in UV–visible absorption spectra (**Figure 3**a–c). It is known that the variation of structure and composition of semiconductor nanocrystal induced by doping would tailor the electronic structure and also the optical absorption properties. In general, surface doping, characterizing with nonuniform or disordered distribution of dopant in the surface of host nanocrystal, only generates localized states in the bandgap to cause an increased absorption of additional shoulder-like tail without changing the intrinsic optical absorption edge. In contrast, homogeneous doping with the uniform and ordered dopant distribution in the framework is capable of reconstructing new band structure to induce the overall shift of intrinsic optical absorption edge with exactly parallel to that of pristine ones.[3] The intrinsic absorption edges were shifted from 380, 385, 365, and 360 nm to 390, 395, 380, and 430 nm upon homogeneous carbon doping for TiO_2, ZnO, and BiOCl with exposed {001} or {010} facet, respectively. The nearly parallel shift characteristics of their extended absorption edge can be generally considered as the formation of a narrowed band-to-band excitation pathway caused by the construction of new band structure,[4b] which was further supported by our theoretical calculation results (Figure S4, Supporting Information). For comparison, the surface carbon doped samples were synthesized at a relatively lower calcination temperature of 300 °C. As expected, only shoulder-like light absorption bands at longer wavelength without changing the intrinsic optical absorption edge were observed (Figure 3a–c), reflecting their inhomogeneous distribution of carbon dopants. Therefore, we conclude our general homogeneous carbon doping strategy comprised of the bottom-up hydrothermal processing and the subsequent thermal treatment could effectively realize the uniform and ordered distribution of carbon dopant in the framework of TiO_2, ZnO, and BiOCl. We also found that the increase of light absorption range in homogeneous carbon doped TiO_2, ZnO, and BiOCl was originated from the lift of valence-band maximum induced by the homogeneous incorporations of carbon dopants, as confirmed by Mott–Schottky and valence-band XPS results (Figure S5, Supporting Information). We further noted that, in addition to the extension of light-response range, the improvement of photoinduced charge separation and transfer efficiency was also achieved by this homogeneous carbon doping, as revealed by carbon doping triggered decrease of arc radius shown in electrochemical impedance spectroscopy (Figure S6, Supporting Information). As the photogenerated current could reflect the amount of surviving electrons during the competitive processes of separation-transfer and recombination of photogenerated electrons and holes,[11] the enhanced transient photocurrent response demonstrated the separation and transfer efficiency of photoinduced charge was improved by the homogeneous carbon doping (Figure S7,

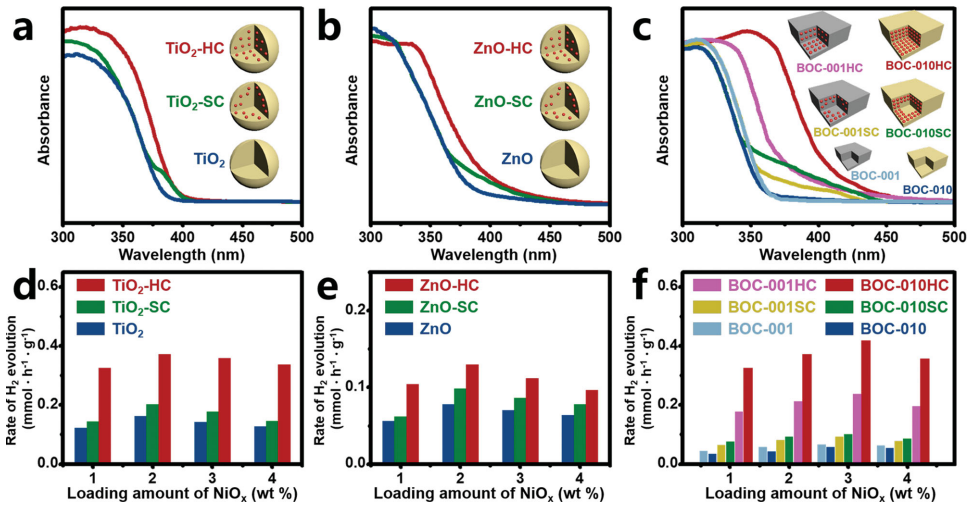

Figure 3. UV–visible absorption spectra of pristine and carbon-doped a) TiO_2, b) ZnO, and c) BiOCl with exposed {001} and {010} facet. Rate comparison of photocatalytic hydrogen evolution over pristine and carbon-doped d) TiO_2, e) ZnO, and f) BiOCl with exposed {001} and {010} facet, using 10 vol% triethanolamine (TEOA) as sacrificial electron donor and NiO_x (1–4 wt%) as co-catalyst.

Supporting Information), which is consistent with theoretical calculation results (Figure S4, Supporting Information). The enhancement of photoinduced charge separation and transfer efficiency could be further evidenced by the quenching of photoluminescence signals of carbon-doped samples in comparison with those of pristine ones (Figure S8, Supporting Information). More importantly, we observed that {010}-facet dominant BiOCl nanosheets exhibited much higher light absorption capacity and charge separation efficiency, as suggested by their extended absorption range, improved electronic conductivity, and enhanced transient photocurrent response with respect to those of {001} facet-dominant counterparts. These property differences in both optical absorption and electrochemical measurements for BiOCl nanosheets with exposed {001} or {010} facet might originate in their facet dependence of homogeneous carbon doping.

2.3. Effect of Homogeneous Carbon Doping on Solar-to-Hydrogen Conversion Efficiency

Encouraged by the theoretical and experimental elucidation of the improvement of both light absorption and charge separation-transfer associated with homogeneous carbon doping, we therefore investigated the effects of homogeneous carbon doping on the solar to hydrogen energy conversion over these catalysts loaded with NiO_x co-catalyst with using the hole scavenger triethanolamine (TEOA) as the sacrificial electron donor under simulated solar light irradiation.[12] A control experiment only with added TEOA and NiO_x co-catalyst showed that no hydrogen was generated in the absence of photocatalysts even after 5 h of light irradiation. Pristine samples without NiO_x loading also exhibited negligible photocatalytic hydrogen evolution activities (Figure S9, Supporting Information). Even with the assist of NiO_x loading, the photocatalytic hydrogen evolution rates of undoped samples were still quite low presumably due to their poor light-harvesting and sluggish charge-carrier transportation (Figure 3d–f). Despite the extension of solar absorption, surface carbon doping only slightly increased the photocatalytic hydrogen evolution performance of the catalysts because concomitantly generated lattice defects could serve as the recombination centers of photogenerated carriers. As expected, the homogeneous carbon doping remarkably boosted the photocatalytic hydrogen generation rates of TiO_2, ZnO, and BiOCl with the different loading amounts of NiO_x co-catalyst from 1 to 4 wt%. The hydrogen production rates reached the maximum values of 0.37 and 0.13 mM h^{-1} g^{-1} for TiO_2 and ZnO at 2 wt% of NiO_x loading, whereas the 3 wt% of NiO_x loading on the {001}- or {010}-faceted BiOCl nanosheets gave rise to the highest photocatalytic hydrogen evolution rates of 0.24 and 0.42 mM h^{-1} g^{-1}, respectively. Too much loading of NiO_x co-catalyst would decrease the hydrogen evolution rate, presumably due to the shielding effect of excess NiO_x.[13] This nonlinear relationship of photocatalytic activity with loading amounts of NiO_x co-catalyst ruled out the contribution of co-catalyst on the improved hydrogen evolution rate, but indicated that the photoactivity enhancement was solely attributed to the homogeneous carbon doping.

We found that the homogeneous carbon doping could more remarkably promote the photoactivity hydrogen evolution ability of BiOCl, as demonstrated by their 3.6 (BOC-001HC) and 8.1 (BOC-010HC) times rate enhancement, significantly higher than those (2.5 and 1.7 times) of TiO_2 and ZnO. These results revealed that the homogeneous carbon doping could enhance the solar-to-hydrogen conversion efficiency. More interestingly, the carbon doped BiOCl nanosheets of {010} facet exposure were much more effective for photocatalytic hydrogen generation than the {001} counterparts, suggesting their facet dependent solar-to-hydrogen conversion property was arisen from the facet dependent carbon doping behavior. Our previous reports demonstrated that BiOCl nanosheets of {001} facet exposure possessed the enhanced photocatalytic organic pollutant degradation ability under UV light because of the suitable internal electronic field induced by the unique

layered structure favored the separation of photogenerated carriers.[9a,c,11] To evaluate the facet effect on the photoreactivity, we prepared a reference BiOCl nanosheets with {010} facet exposure and 0.51% of carbon doping (named as BOC-010HC-1), the same carbon doping amount as that of BOC-001HC. TEM, HRTEM, and selected-area electron diffraction (SAED) analyses of BOC-010HC-1 demonstrated its {010} facet exposure (Figure S10, Supporting Information). BOC-010HC-1 exhibited lower photocatalytic hydrogen evolution performance than BOC-001HC under the same loading amounts of NiO_x cocatalyst, suggesting that the facet exposure influenced the photoreactivity even with the same amount of carbon dopants and the preferential exposure of {001} facet was more beneficial for the photocatalytic hydrogen evolution. The photocatalytic hydrogen evolution activity of BOC-010HC with 2.98% of carbon dopants was much higher than that of BOC-010HC-1 with 0.51% of carbon dopants (Figure S10f, Supporting Information), confirming that the carbon dopant amount was crucial for the photocatalytic hydrogen evolution activity of carbon doped BiOCl nanosheets with the same facet exposure. As the final carbon doping amounts in BiOCl nanosheets were strongly dependent on their facet exposure and the photocatalytic hydrogen evolution activity of carbon doped BiOCl nanosheets was related to their carbon doping amounts, it is reasonable for us to conclude that the solar-to-hydrogen conversion property of carbon doped BiOCl nanosheets is facet dependent. Meanwhile, these results further reflected the negligible effect of {001} facet-related internal electronic field under solar light of tiny UV light, but highlighted the crucial role of homogeneous carbon doping in promoting the solar-to-hydrogen conversion.

2.4. Homogeneous Carbon Doping Mechanism

Motivated by the successful facet-controllable synthesis of homogeneous carbon doped BiOCl nanosheets as well as their interesting facet-dependent carbon doping behavior and solar-to-hydrogen conversion property, we attempted to clarify the underlying doping mechanism at a crystal facet level with using {001}- and {010}-faceted homogeneous carbon doped BiOCl nanosheets as the examples.

It is well-established that the doping process of nanocrystal usually involves the adsorption of dopant precursor on the host crystal surface, their subsequent diffusion from the surface to the bulk, and ultimate incorporation of dopant to the substitution sites.[5] Obviously, clarifying the homogeneous carbon doping mechanism relies on elucidating the detailed transfer pathway of elemental carbon through addressing the issues as follows. How did the dopant precursors adsorb on and/or interact with the host substrates and then diffuse from the outer to interior? How did the carbon dopants substitute for the lattice atoms? What roles did the hydrothermal processing and thermal treatment play during the whole doping process?

2.4.1. Carbon Transfer during Hydrothermal Processing

To clarify the transfer pathway of elemental carbon during hydrothermal processing, we should first check the chemical states and spatial distributions of elemental carbon in carbonaceous modified BiOCl nanosheets (Scheme S1, Supporting Information). Previous reports demonstrated that the XPS depth profiling technique (also time-dependent XPS spectra) with Ar^+ sputtering was able to address this issue.[14] For instance, Cheng and co-workers identified the gradient distribution of elemental boron from the core to the shell of an anatase TiO_2 with using this technique.[14a] We therefore used time-dependent XPS to investigate the change of high resolution C 1s XPS peak signals of carbonaceous modified BiOCl nanosheets upon Ar^+ sputtering from 0 to 1200 s. Prior to Ar^+ sputtering, three peak signals at 284.6, 286.3, and 288.6 eV were observed in the high resolution carbon XPS spectra of CBOC-001 and CBOC-010 (**Figure 4**a2,b2), which were typically assigned to sp^2 hybridized C—C, C—O, and C═O bonds, respectively. These assignments of XPS peak of C signals were consistent with the previous reports.[15] The XPS analysis result revealed the presence of carbonaceous species on the BiOCl surface after the hydrothermal processing. The peak intensity of C—C bonds in CBOC-010 and carbon–oxygen (C—O and C═O) bonds in CBOC-001 did not change during the Ar^+ sputtering from 0 to 120 s. This observation suggested that hydrothermal processing favored the deposition of the carbonaceous species on the surface of BiOCl and their subsequent implantation into its shallow lattice, which was confirmed by the retention of XPS peak signals of C—C bonds and carbon–oxygen bonds upon 240 s Ar^+ sputtering in the two carbon-modified samples. We interestingly found that the binding modes of carbonaceous species implanted into the inner shallow lattice were highly dependent on the facet exposure of BiOCl (Figure 4a1,b1), as reflected by XPS results and ^{13}C NMR spectra (Figure 4a3,b3).[16] Because of the oxygen-terminated nature of BiOCl {001} facet and the strong affinity of carbonaceous species to oxygen atom,[12b,17] carbonaceous species implanted into the {001} facet were prone to interact with oxygen atoms to form C—O and C═O bonds, as proven by the retention of carbon–oxygen bonds signals upon 240 s Ar^+ sputtering. It is known that the interleaved stacks of $[Bi_2O_2]$ and [Cl] slices by the van der Waals interaction of chlorine atoms along the [001] orientation usually results in the generation of unique layered structure in BiOCl, which also endowed its {010} facet with open channel characteristic.[9] These layered structure mediated open channels could provide suitable accommodation space for the intercalated nanomaterials to form sandwich-like analogues such as silica pillared $Ca_2Nb_3O_{10}$, Brønsted acids intercalated h-BN, and so on.[18] Similarly, the implanted carbonaceous species were intercalated between the neighboring $[Bi_2O_2]$ layers of CBOC-010. Obviously, these carbonaceous species could be intercalated more deeply along the open channels formed between the $[Bi_2O_2]$ stacks of CBOC-010 than against the $[Bi_2O_2]$ stacks of CBOC-001, which was validated by the longer existence of C—C bonds signals of CBOC-010 even upon 360 s Ar^+ sputtering than the case (240 s) of CBOC-001. As the sputtering time increased from 480 and 1200 s, all the C 1s signals of CBOC-001 and CBOC-010 disappeared, further confirming that the implanted carbonaceous species only existed in the shallow lattice of BiOCl. Subsequently, we utilized plasma treatment to remove the surface modified carbonaceous species of CBOC-001 and CBOC-010 to respectively obtain PBOC-001 and PBOC-010 (Scheme S3, Supporting Information) only

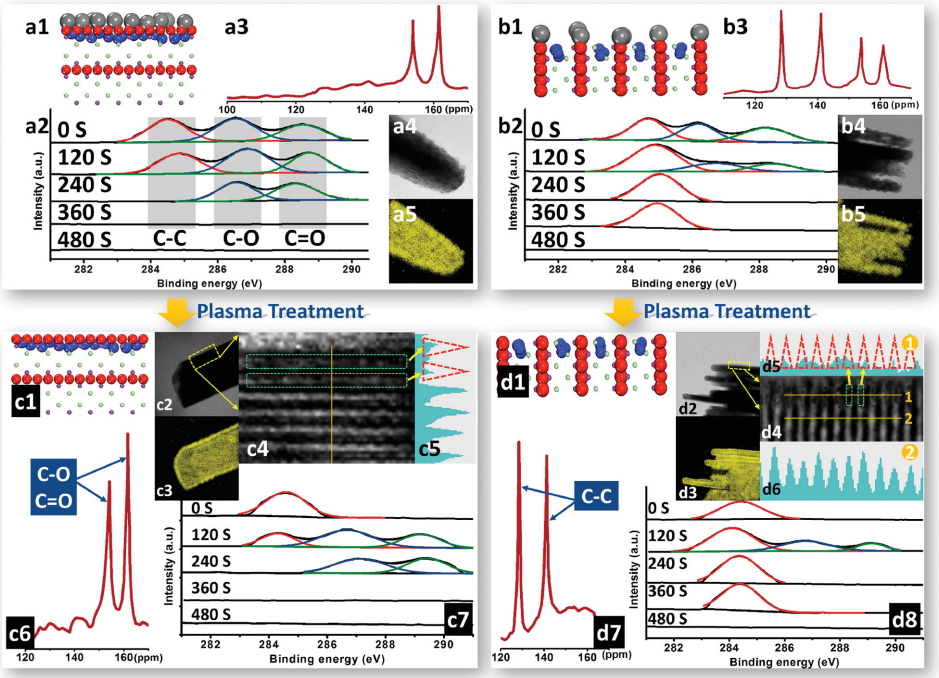

Figure 4. Characterizations of the chemical states and spatial distributions of elemental carbon in a1–a5) CBOC-001, b1–b5) CBOC-010, c1–c7) PBOC-001, and d1–d8) PBOC-010. a1, b1, c1, d1) Schematic illustration of the adsorption modes of carbonaceous species. a2, b2, c7, d8) Time-dependent high resolution C 1s XPS spectra upon Ar^+ sputtering. a3, b3, c6, d7) ^{13}C NMR spectra. a4, b4, c2, d2) TEM images. a5, b5, c3, d3) Elemental mapping images. c4, d4) HRTEM images taken from (c2) and (d2), respectively. c5, d5, d6) Intensity profiles along the lines in image (c4) and (d4), respectively. Plasma treatment of CBOC-001 and CBOC-010 (Scheme S1, Supporting Information) synthesized by bottom-up hydrothermal processing resulted in the formation of PBOC-001 and PBOC-010 (Scheme S3, Supporting Information), respectively.

with implanted carbonaceous species in the shallow lattice, aiming to eliminate the undesired disturbance of surface modified carbonaceous species on the characterization results of the implanted carbonaceous species in the shallow lattice.[19] The dramatic changes from the rough surface of CBOC-001 (Figure 4a4) and CBOC-010 (Figure 4b4) to the smooth surface of PBOC-001 (Figure 4c2) and PBOC-010 (Figure 4d2) revealed the successful removal of the surface modified carbonaceous species by the plasma treatment. Different from the homogeneous distribution nature of carbon in CBOC-001 (Figure 4a5) and CBOC-010 (Figure 4b5), the elemental mappings of PBOC-001 (Figure 4c3) and PBOC-010 (Figure 4d3) exhibited sheath-like distribution of carbon, verifying the existence of carbonaceous species in their shallow lattices. HRTEM characterization was employed to further confirm the XPS analysis results. In the HRTEM images of PBOC-001 (Figure 4c4), the darkening of the interlamellar space between the first three layers near the surface demonstrated the adsorption of carbonaceous species underneath the {001} facet, which was also evidenced by the absence of the two peak signals in the top of their intensity profiles (Figure 4c5). ^{13}C NMR spectra revealed that these implanted carbonaceous species mainly interacted with lattice oxygen to yield C—O or C=O bonds (Figure 4c6).[16] In contrast, the HRTEM images of PBOC-010 showed the clear sandwich-like intercalation of carbonaceous species in the shallow lattice (Figure 4d4). Intensity profiles taken from the region of carbonaceous species intercalation gave no peak signals (Figure 4d5). When the intensity profiles was taken from the bulk region, periodic peak arrays emerged (Figure 4d6). As for PBOC-010, only the signals of C—C bonds were observed (Figure 4d7),[16] further identifying the sandwich-like intercalation of carbonaceous species in the shallow lattice, consistent with their adsorption modes (Figure 4d1). As shown in the XPS spectra of PBOC-001 (Figure 4c7) and PBOC-010 (Figure 4d8), the peak signals of carbon–oxygen (C—O and C=O) bonds were absent at 0 S Ar^+ sputtering, validating the disappearance of surface deposited carbonaceous species arisen from the plasma treatment. Upon 120–360 S Ar^+ sputtering, the retention of carbon–oxygen (C—O and C=O) bonds in PBOC-001 and C—C bonds in PBOC-010 further evidenced the facet-dependent adsorption of the carbonaceous species in the shallow lattice. These results clearly demonstrated the adsorption modes of implanted carbonaceous species in the shallow lattice highly depended on the facet exposures of BiOCl nanosheets.

The successful elucidation of the chemical states and spatial distributions of elemental carbon in carbonaceous modified BiOCl nanosheets allowed us to further clarify the transfer pathway of elemental carbon during hydrothermal processing. Raman spectrum experiments were then conducted to explore the evolution process of elemental carbon from the glucose molecules to surface-modified and implanted carbonaceous species by investigating the structural change of the samples prepared at different hydrothermal time. Typically, Raman signals of pristine BiOCl give four characteristic bands at 59, 142, 199, and 396 cm^{-1} (**Figure 5**a–d), which are assigned to the A_{1g} internal Bi–Cl stretching mode, the A_{1g} internal

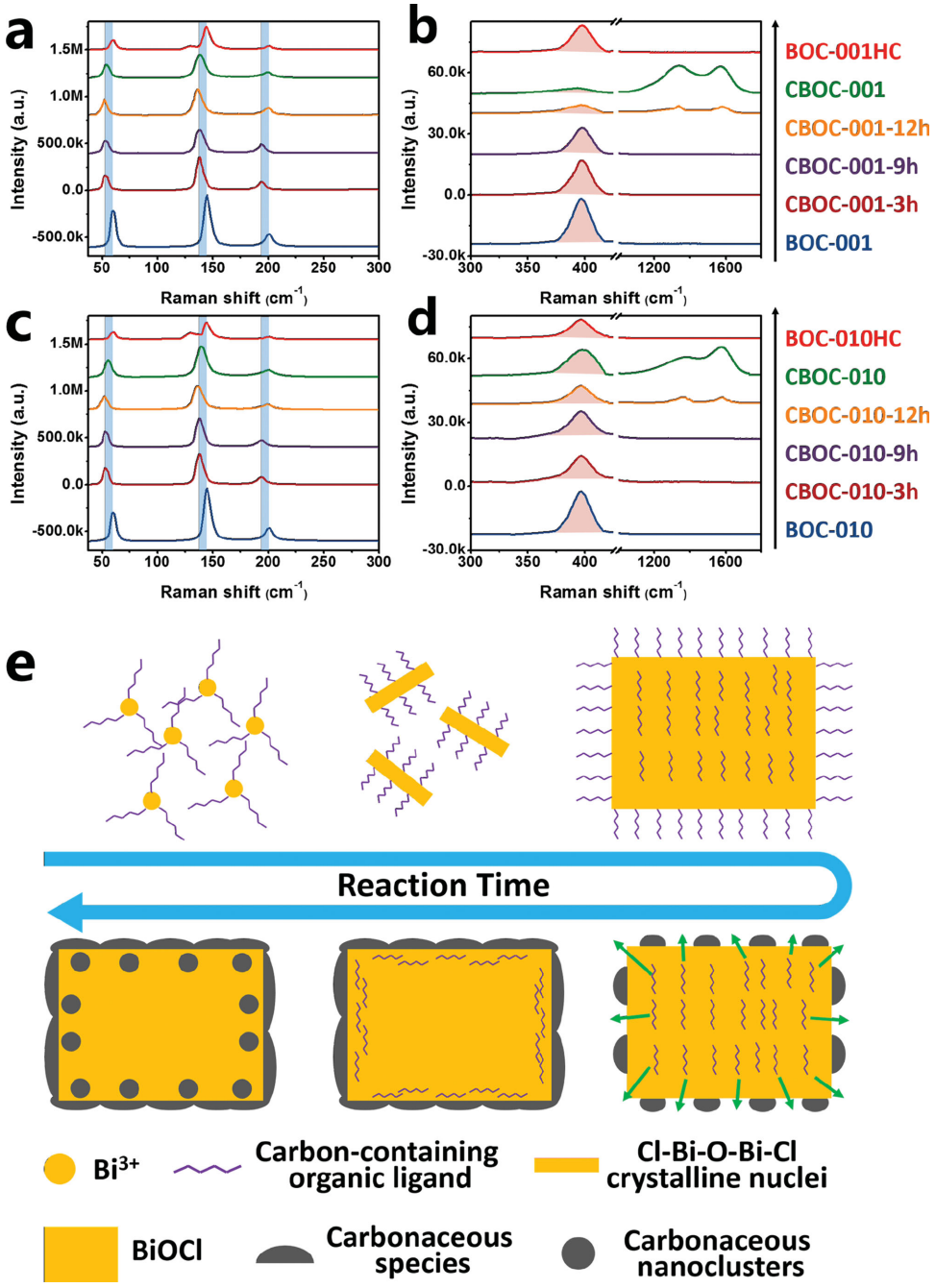

Figure 5. Raman spectrum of carbon-modified BiOCl with the exposure of a,b) {001} and c,d) {010} facets synthesized at different hydrothermal time (using pristine and carbon-doped ones as the comparison). e) Schematic illustration of the formation process of carbonaceous species implanted in the shallow lattice during bottom-up hydrothermal process.

Bi–Cl stretching, and E_g external Bi–Cl stretching mode, the E_g internal Bi–Cl stretching mode, and a weak B_{1g} band corresponds to the motion of the oxygen atoms, respectively.[20,21b] As soon as bismuth nitrate and glucose were dissolved in the aqueous solution, glucose would coordinate with Bi^{3+} cations to generate alkoxides complexes,[9c] which reacted with chlorine ions immediately to generate tiny X–Bi–O–Bi–X crystalline nuclei wrapped with carbon-containing organic ligands under hydrothermal reaction condition (Figure 5e). Subsequently, Ostwald ripening governed the growth of these crystalline nuclei and some key parameters such as surrounding pH, solution viscosity, and reaction temperature directed their oriented assembly into BiOCl intermediates, while the agglomeration of these crystalline nuclei would yield BiOCl nanocrystals implanted by carbon-chain-like species in their interior.[21–22] The corresponding structural change was reflected by the blue shift of the bands at 59, 142, and 199 cm^{-1} in BiOCl nanocrystals synthesized at 3 and 9 h of hydrothermal reaction, which

was indicative of the destruction of lattice symmetry induced by the incorporation of carbon-chain-like species into the lattice of BiOCl. With the proceeding of hydrothermal reaction, the carbon-chain-like species on the surface of BiOCl would be carbonized into surface modified carbonaceous species, while carbon atoms in alkoxides complexes coordinated with Bi in the inner of BiOCl were gradually substituted Cl and/or O of BiOCl. On the other hand, these carbon-chain-like species at deep lattice of BiOCl was expelled outside the lattice of BiOCl because of the lattice self-purification effect.[5] However, the increasing carbonaceous species coverage on the BiOCl surface would gradually block the escape of carbon-chain-like species, resulting in their residual within the shallow lattice of BiOCl. Further hydrothermal treatment to 12 h resulted in the disappearance of the blue-shift of peak signal at 199 cm^{-1}, whereas the similar phenomenon was not observed for the peak signals at 59 and 142 cm^{-1}. This indicated the complete transfer of carbon-chain-like species from the deep lattice to shallow lattice. At the same time the carbonization of these residual carbon-chain-like species occurred, producing the carbonaceous species located in the shallow lattice of BiOCl. This process was evidenced by the emergence of D and G bands at 1343 and 1586 cm^{-1} after 12 h of reaction and their subsequent intensity increment with prolonged reaction time. This also suggested that the implanted carbonaceous species had a size of nanoscale, which was further supported by the control experiments (Figure S12, Supporting Information). It should be noted that, although {001}- and {010}-faceted BiOCl nanosheets underwent the same carbonization process described above, their facet-related surface atomic structures largely regulated the adsorption modes. In the case of {010} facet, the implanted carbonaceous nanoclusters were bound to the shallow lattice oxygen underneath the {001} facet with high density of oxygen, which was confirmed by the abovementioned XPS analysis result and the signal intensity decrease of B_{1g} band with the increment of reaction time arisen from the suppression of oxygen atoms motion (Figure 5a,b). Whereas, for {010} facet, the open channel along [010] orientation provided large accommodation space for the intercalation of carbonaceous species, resulting in the weak affinity of the implanted carbonaceous nanoclusters to oxygen atoms, which was reflected by the slight change in the peak signal of B_{1g} band. When the carbon modified BiOCl samples were subjected to thermal treatment in air, a new bands appeared at 121 cm^{-1}, arising from a new active mode induced by the homogeneous carbon doping.[23]

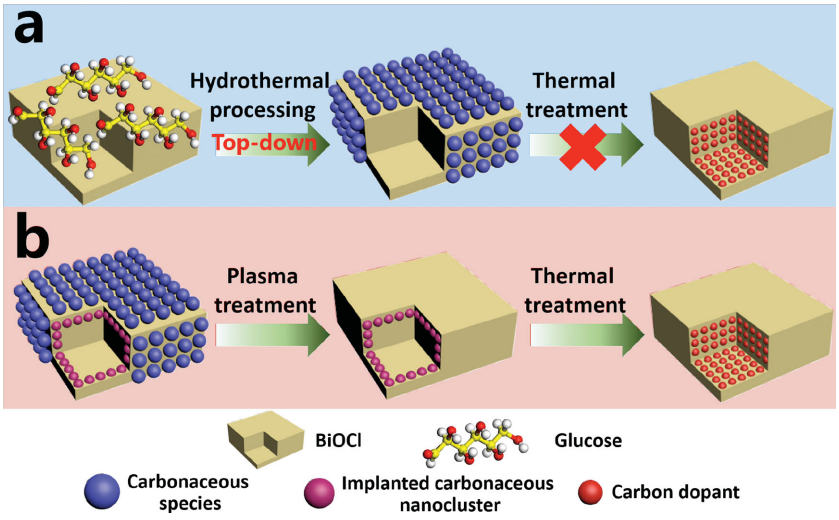

Figure 6. a) Exploration of the contribution of surface modified carbonaceous species to carbon doping. b) Elucidation of the role of implanted carbonaceous nanoclusters during carbon doping.

2.4.2. Carbon Transfer during Thermal Treatment

As both surface modified carbonaceous species and carbonaceous nanoclusters implanted in the shallow lattice existed in BiOCl nanosheets, to understand the carbon transfer process during thermal treatment, we first estimated the contribution of surface modified carbonaceous species to the carbon homogeneous doing by preparing carbon modified BiOCl without the implantation of carbonaceous nanoclusters into the shallow lattice (**Figure 6**a). These carbon modified BiOCl counterparts were obtained by directly reacting pristine {001}- and {010}-faceted BiOCl with glucose at 160 °C for 18 h (called as TBOC-001 and TBOC-010, respectively; Scheme S4, Supporting Information) through a top-down hydrothermal route, one of the conventional doping models. As expected, the carbon–oxygen bonds signals only appeared in the XPS spectra of TBOC-001 before Ar^+ sputtering, while the C—C bonds signals completely disappeared in the XPS spectra of TBOC-010 after 240 s Ar^+ sputtering (Figure S13, Supporting Information). No red-shift in UV–visible absorption spectra was observed for the thermally treated TBOC-001 and TBOC-010 (Figure S14, Supporting Information), presumably due to the burning of surface modified carbonaceous species under the thermal treatment at 450 °C for the carbon dopant diffusion, exhausting the dopant precursor for the subsequent doping procedure. We therefore hypothesized that the implantation of carbonaceous nanoclusters in the shallow lattice of host nanocrystal was vital for the effective homogeneous doping.

To confirm this opinion, CBOC-010 and CBOC-001 were subjected to plasma treatment to remove their surface modified carbonaceous species with preserving the carbonaceous nanoclusters in the shallow lattice (Figures 4 and 6b).[19] As expected, after the subsequent calcination of the plasma treated CBOC-010 and CBOC-001 (called as PBOC-010 and PBOC-001, respectively; Scheme S3, Supporting Information) in air, the same red-shift in optical absorption spectrum as that of BOC-001HC and BOC-010HC appeared (Figure S15, Supporting Information), solidly confirming that these carbonaceous nanoclusters implanted in the shallow lattice served as the carbon dopant precursor for the subsequent thermal-induced homogeneous carbon doping.

Although the source for the homogeneous carbon doping in BiOCl has been clarified, it is still unclear which kind of

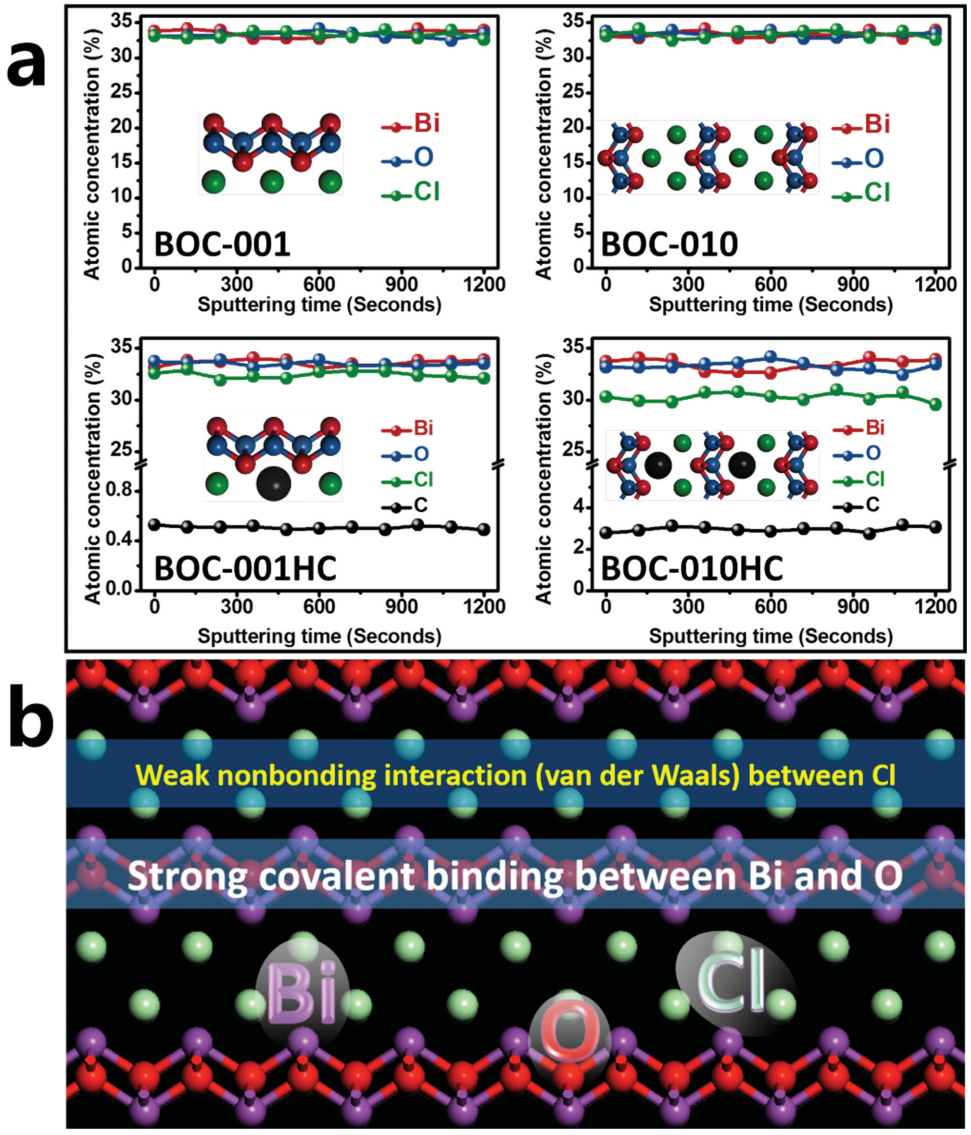

Figure 7. a) X-ray photoelectron spectroscopy depth profiling of pristine and carbon-doped BiOCl demonstrating the concentrations of their component elements. b) Schematic illustration of the unique layered structure of BiOCl explaining why carbon dopant substituted for lattice chlorine.

lattice atoms carbon dopant substituted for. To address this issue, the concentrations of different elements in BOC-001HC and BOC-010HC were determined by normalizing XPS peak area with atomic sensitivity factor according to Equation (1). The almost unchanged atomic concentration of carbon upon long time sputtering further confirmed the homogeneous distribution of carbon dopant within the whole crystal lattice of BiOCl (**Figure 7**). Moreover, the relatively low concentration of chlorine with respect to that of bismuth and oxygen provided a strong evidence of chlorine substitution by carbon. As mentioned previously, BiOCl crystallized into unique layered structures consisting of [Cl–Bi–O–Bi–Cl] slices stacked together by the van der Waals interaction between the halogen atoms along the c-axis. Obviously, compared to the strong covalent binding between Bi and O, the weak van der Waals interaction of Cl favored its substitution by carbon energetically.[21]

The successes in exploring the origin and destination of carbon dopant precursor allowed us to gain insight into the diffusion and substitution process of carbon dopant in detail. We therefore carried out a quantitative analysis of carbon transfer during the doping process shown in **Figure 8**. These equations demonstrated that the doping efficiency was determined by implantation efficiency and diffusion–substitution efficiency. The calculated efficiency values were summarized in Table S1, Supporting Information. For the implantation of carbonaceous nanoclusters in the shallow lattice, the efficiency (α = 5%) of {001}-faceted BiOCl nanosheets was slightly higher than that (α = 4%) of {010}-faceted counterparts (Figure 8a). Therefore, when 2.22 mM glucose (13.32 mM of carbon) was used as the carbon sources, 0.86 mM of carbon source was modified as carbonaceous species on the surface of {001} dominated nanosheets, and 0.68 mM of carbon source was implanted as carbonaceous nanoclusters into the shallow lattice of {001}

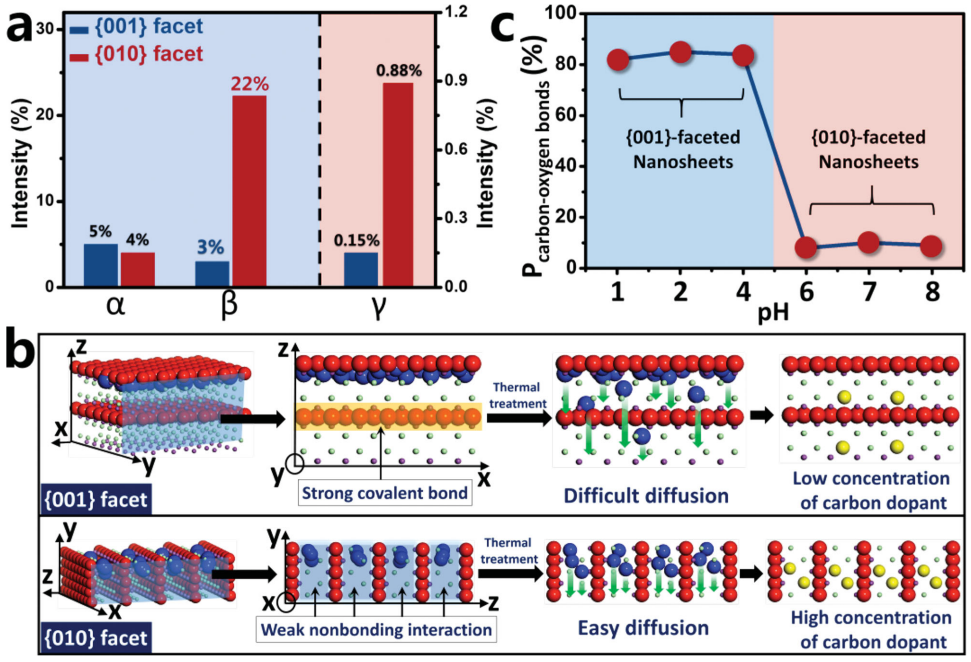

Figure 8. a) Comparison of the implantation efficiencies of carbonaceous nanoclusters (α), the diffusion–substitution efficiencies (β), and the doping efficiencies (γ) of {001}- and {010}-faceted carbon doped BiOCl. These parameters were obtained from the following equations: α = B/A, β = C/B, and γ = C/A, where A, B, and C are the carbon contents in glucose reactants, carbonaceous nanoclusters, and carbon dopants in BiOCl, respectively, and calculated on the basis of Equation (1) described above. b) Schematic illustration of the detailed carbon doping process of {001}- and {010}-faceted BiOCl accounting for the role of facet-related arrangement of bulk atom on the diffusion and concentration of carbon dopant. c) Percentages of carbon–oxygen bonds ($P_{carbon–oxygen\ bonds}$) in the carbonaceous species implanted into the shallow lattice of carbon-modified BOCl synthesized via the bottom-up hydrothermal route at different pH values.

dominated nanosheets. As for the {010} counterparts, 0.71 mM of carbon source was modified as carbonaceous species and 0.54 mM of carbon source was implanted as carbonaceous nanoclusters, respectively. The higher amount of implanted carbonaceous nanoclusters in the shallow lattice of {001} faceted BiOCl nanosheets might be arisen from the dense arrangement of oxygen atoms exposed on {001} facet and the strong affinity of carbonaceous nanoclusters to oxygen, which enabled their strong bonding with each other to go against the self-purification mediated removal of carbonaceous nanoclusters implanted in the shallow lattice during the hydrothermal process. When the dopant precursor contained BiOCl nanosheets were subjected to calcination in air, thermal treatment provided sufficient energy to trigger the decomposition of carbonaceous species into carbon dopant and simultaneously overcome the energy and space barrier for the subsequent substitution of lattice chlorine atoms with carbon atoms. For the {001} facet-dominating BiOCl nanosheets, dopant precursor were mainly close to the inner lattice oxygen of {001} facet and the carbon atoms must first traverse $[Bi_2O_2]$ layers to subsequently substitute for chlorine (the top part of Figure 8b). The strong covalent binding between Bi and O as well as their highly dense arrangement in $[Bi_2O_2]$ layers would strongly inhibit the diffusion of carbon dopant, resulting in a low diffusion–substitution efficiency of 3%. In contrast, the diffusion–substitution efficiency of {010} facet-dominating nanosheets was as high as 22%, more than 7 times that of {001} counterparts. This dramatic diffusion–substitution efficiency enhancement was first related to the open channels of {010}-faceted BiOCl, which could provide expedite diffusion pathway for the facile transfer of carbon dopant to the substitution sites. Meanwhile, the weak van der Waals interaction among the chlorine atoms along [010] crystal orientation favored the carbon dopant diffusion and the subsequent chlorine substitution by carbon (the bottom part of Figure 8b). These two reasons accounted for the higher doping efficiency of BOC-010HC, although its uncalcined precursor (CBOC-010) possessed a relatively lower amount of carbonaceous nanoclusters implanted in the shallow lattice. Obviously, the higher concentration of carbon dopant endowed {010}-faceted BiOCl with extended solar absorption range and improved charge transportation, and thus with enhanced solar-to-hydrogen conversion.

To check whether the pH value of synthetic solutions directly affected the adsorption modes of implanted carbonaceous species in the shallow lattice, we therefore synthesized {001}-faceted carbon-modified BiOCl at pH = 1, 2, 4 and {010}-faceted counterpart at pH = 6, 7, 8 (Figure S16, Supporting Information). The adsorption modes of implanted carbonaceous species were determined by calculating the percentages ($P_{carbon–oxygen\ bonds}$) of carbon–oxygen bonds in the carbonaceous species implanted into the shallow lattice of carbon-modified BOCl. We thus plotted $P_{carbon–oxygen\ bonds}$ versus pH as Figure 8c. Instead of a continuous linearity- or parabola-like curve of strong interdependency, only the discontinuous relationship between $P_{carbon–oxygen\ bonds}$ and pH was observed (Figure 8c), suggesting the negligible influence of pH value on the adsorption of implanted carbonaceous species. As expected, $P_{carbon–oxygen\ bonds}$ showed strong dependence on the facet exposure. These results suggested that it was not the pH value, but the facet exposure

to determine adsorption modes of implanted carbonaceous species, although the pH value was capable of governing the facet exposure when it was shifted from 1–4 to 6–8.

2.4.3. New Doping Model Based on the Dopant Precursor Implantation in the Shallow Lattice of Host Nanocrystal

On the basis of the above results, we conclude that the first step (bottom-up hydrothermal processing) of our general homogeneous carbon doping strategy allows the implantation of carbon dopant precursor in the shallow lattice of BiOCl, while the second step (thermal treatment) triggers the diffusion of carbon dopant to substitute for host lattice atom, leading to the formation of homogeneous carbon doping. Among them, the dopant precursor implantation in the shallow lattice of host nanocrystal is vital for the effective homogeneous doping.

To confirm the importance of dopant precursor implantation in the shallow lattice of host nanocrystal, we designed a series of control experiments to investigate the correlation of the implanted dopant precursor amounts with the final dopant concentration with using {010} facet-dominant BiOCl nanosheets as the model material. We tuned the concentration of carbonaceous nanoclusters implanted in the shallow lattice of BiOCl by controlling the dosage of glucose and the hydrothermal conditions such as reaction time and temperature (Table S2, Supporting Information). The obvious linear relationship of the implanted dopant precursor amounts with the final dopant concentration was observed (**Figure 9**a), confirming that the dopant precursor implantation in the shallow lattice of host nanocrystal was vital for the effective homogeneous doping.

These mechanistic insights also suggest a new doping model based on the dopant precursor implantation in the shallow lattice of host nanocrystal in this study (Figure 9b). This model is different from the conventional doping model based on the organic ligands or gas molecules adsorption onto the surface of host nanocrystals.[24] In the case of conventional doping model, strong adsorption capacity of dopant precursor toward the surface of host nanocrystal are highly required for the effective doping. However, the actual poor binding ability of most nanocrystals to surface trapped dopant precursor resulted in a low doping efficiency and/or surface doping. In comparison with the conventional doping model, our new doping model possesses three advantages for the effective homogeneous doping. First, the dopant precursor implantation in the shallow lattice can provide persistent dopant source, facilitating the emergence of homogeneous doping. Second, the lattice of host nanocrystal could avoid the loss of dopant precursor caused by uncontrollable burning during thermal treatment. This is because much higher temperature operation is required to activate the dopant for diffusion and substitution in the conventional doping model, which inevitably decompose dopant precursor exposed on the surface, as revealed by the case of carbon modified BiOCl prepared with a top-down route (Figure 6a). Finally, the implantation of foreign carbon into the shallow lattice would destruct the lattice symmetry and thereby weaken the bonds of host nanocrystal, favoring the subsequent carbon substitution. The proposed mechanism was supported by the positive correlation of diffusion–substitution efficiency (β) with

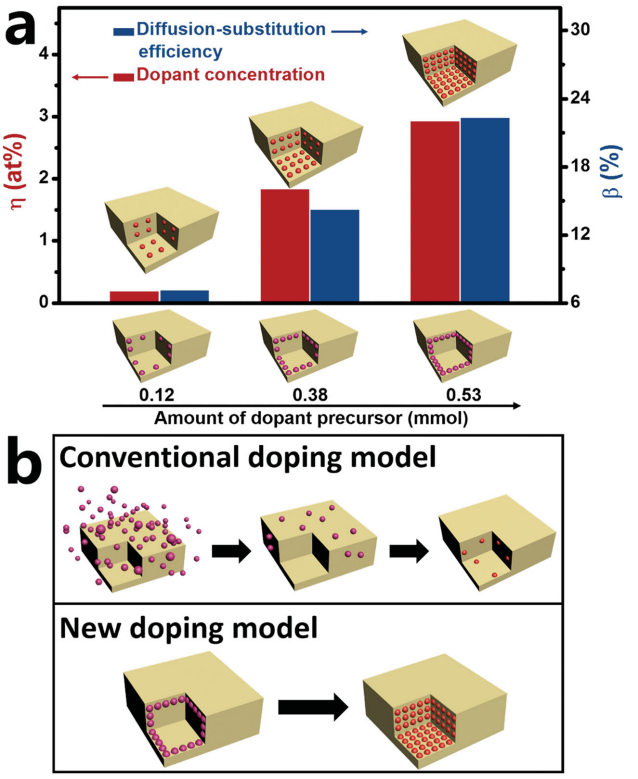

Figure 9. a) The correlation of the diffusion–substitution efficiency β and the dopant concentration η with the dopant precursor (implanted carbonaceous nanoclusters) amounts in new doping model with using {010} facet-dominant BiOCl nanosheets as the model material. b) Schematic illustration of the conventional doping model reported before and the new doping model established here.

the dopant precursor amounts (Figure 9), because the implantation of more carbonaceous nanoclusters into the lattice could provide more dopant precursor and thus more seriously destruct the lattice symmetry than the convenient dopant diffusion–substitution. As expected, this new doping model could also be applicable to TiO_2 and ZnO (Figure S17, Supporting Information).

3. Conclusions

In summary, we report a general homogeneous carbon doping strategy comprised of pre-hydrothermal carbonization processing and subsequent thermal treatment. The choice of this doping strategy for mechanistic investigation was encouraged by its versatility, not only in enabling homogeneous incorporation of carbon, but also in improving solar-to-hydrogen conversion theoretically and experimentally, for typical oxides including TiO_2, ZnO, and BiOCl. With using the well-defined BiOCl nanosheets of high {001} or {010} facet exposure, we clarified the homogeneous carbon doping mechanism at a crystal facet level for the first time. The initial hydrothermal-induced implantation of dopant precursor of carbonaceous nanoclusters into the shallow lattice was regulated by the facet-related surface atomic structure and vital for the effective

homogeneous doping, which differentiated this new doping model from the conventional doping model based on the organic ligands or gas molecules adsorption onto the surface of host nanocrystals. When the subsequent thermal treatment proceeded, facet-related arrangement of bulk atom was identified as the key factor to determining the diffusion of carbon dopant, which governed the ultimate concentration of carbon dopant and thereby the efficiency of solar-to-hydrogen conversion in BiOCl nanosheets. This study sheds light on the underlying doping mechanism to enrich fundamental theory of doping chemistry and these mechanistic insights open up new opportunities for the design and synthesis of high-performance doped photocatalysts.

4. Experimental Section

Sample Preparation: In a typical procedure, 2.22 mM of glucose and 4 mM of $Bi(NO_3)_3$, or $Ti(SO_4)_2$, or $Zn(NO_3)_2$ were ground together for 30 min in an agate mortar. Then the mixtures were added slowly into distilled water under ultrasonication to give a transparent solution. To synthesize the carbon doped TiO_2, the mixture solution was directly transferred to a 100 mL Teflon-lined stainless autoclave for the subsequent hydrothermal processing. As for the carbon doped ZnO, 8 mL of 1 M L^{-1} NaOH was added into the mixture solution before the hydrothermal processing. For the synthesis of the carbon doped BiOCl, 4 mM of KCl was added into the mixture solution, followed with adjusting the pH value to 1 or 6 by adding 1 M L^{-1} HNO_3 or NaOH solution prior to hydrothermal processing. Hydrothermal treatment of the final solutions at 160 °C for 18 h produced different kinds of carbon-modified samples, which were called as $CTiO_2$, CZnO, CBOC-001 (pH = 1) and CBOC-010 (pH = 6), respectively. These carbon-modified samples were then subjected to thermal treatment in air at 300 °C or 450 °C for 4 h, which formed the surface C-doped samples and the homogeneous C-doped samples, respectively. We called the surface C-doped samples as TiO_2-SC, ZnO-SC, BOC-001SC, and BOC-010SC, while the homogeneous C-doped samples as TiO_2-HC, ZnO-HC, BOC-001HC, and BOC-010HC, respectively. In some cases, plasma treatment was used to remove their surface-absorbed carbonaceous species. For comparison, pure TiO_2, ZnO, and BiOCl with {001} or {010} facet exposure were synthesized with the aforementioned method in the absence of glucose. The resulting BiOCl with {001} or {010} facet exposure were called as BOC-001 and BOC-010, respectively. The preparation process and the names of all the samples involved in this study were summarized in Scheme S1–8, Supporting Information. The loading of NiO_x cocatalyst was conducted using an impregnation method.[12] Typically, the as-prepared sample was first dispersed in an aqueous $Ni(NO_3)_2$ solution and heated in a water bath under constant stirring until the water was completely evaporated. The resulting powder was dried at 50 °C in air, followed with thermal treatment at 200 °C for 2 h, and then reduced under H_2 flow at 300 °C for 2 h, and finally re-oxidation under O_2 flow at 200 °C for 1 h for the loading of NiO_x.

Characterization: The powder X-ray diffraction (XRD) patterns of the samples were recorded on a Bruker D8 Advance diffractometer with monochromatized Cu Kα radiation (λ = 0.15418 nm). The morphology of the samples was observed with a JEOL JSM-2010 high-resolution transmission electron microscopy (HRTEM). For the TEM sample preparation, the powders were suspended in ethanol, and then a drop of this suspension was deposited onto a holey carbon film supported by a copper grid and then dried in air prior to the TEM examination. UV–visible diffused reflectance spectra of the samples were obtained for the dry-pressed film samples with using a UV–visible spectrophotometer (UV-2550, Shimadzu, Japan) with $BaSO_4$ as the reflectance standard. Chemical compositions and states were analyzed using X-ray photoelectron spectroscopy (XPS) (Thermo Scientific ESCLAB 250Xi). All binding energies were referenced to the C 1s peak (284.6 eV) arising from the adventitious carbon. Atomic concentrations were calculated by normalizing peak areas to the elemental sensitivity factor. Raman measurements were carried out by a confocal laser micro-Raman spectrometer (Thermo DXR Microscope, USA). The laser was 633 nm with a power of 5 mW. EDX elemental mapping (JEOL ARM-200F) was employed to visualize the elemental compositions of the products. Photoluminescence (PL) spectra of the samples were recorded on a Fluoromax-Pluminescence spectrometer (Horiba Jobin Yvon Inc.). ^{13}C and NMR measurements were obtained with a 400 MHz NMR spectrometer (Bruker, Germany) at 298 K.

Photocatalytic H_2 Generation: The photocatalytic hydrogen production experiments were performed at ambient temperature and atmospheric pressure using 500 W Xe arc lamp as the light source. Typically, a 0.05 g of photocatalyst was dispersed in 80 mL of aqueous solution containing 10 vol% triethanolamine scavenger in a 100 mL Pyrex flask sealed with a silicone rubber septum. Prior to irradiation, the suspensions were bubbled with nitrogen for 30 min to remove the dissolved oxygen and to ensure the anaerobic conditions of the reaction system. During the whole reaction process, the aqueous solution with photocatalyst was continuously stirred by a magnetic stirrer. The generated hydrogen gas was sampled by a syringe and measured by a gas chromatography (GC-14C, Shimadzu, Japan) equipped with a thermal conductivity detector (TCD), where Ar was used as a carrier gas.

Electrochemical Measurements: The photoelectrodes were prepared according to our previously reported method.[9a] The indium doped tin oxide (ITO, China Southern Glass Co., Ltd., Shenzhen, China) substrates were first ultrasonically cleaned in distilled water, absolute ethanol, and isopropanol for 15 min sequentially. Both edges of the conducting glass substrates were then covered with adhesive tape. Typically, the aqueous slurries of the samples were spread on an ITO glass substrate with a glass rod, using adhesive tapes as spaces. The suspension was prepared by grinding 20 mg of samples, 40 µL of PEDOT-PSS (Sigma-Aldrich, 1.3%–1.7%) aqueous solution, and 200 µL of water. The resulting film was dried in air and annealed at 150 °C for 10 min. The photocurrents were measured by an electrochemical analyzer (CHI660D, Shanghai, China) in a standard three-electrode system with the samples as the working electrodes, a Pt foil as the counter electrode, and a saturated calomel electrode (SCE) as a reference electrode. A 500 W Xe arc lamp was utilized as a light source. A 0.5 M $Na2SO_4$ aqueous solution was used as the electrolyte.

Computational Methods: Theoretical calculations were performed by the density functional theory (DFT) implemented in the CASTEP code. The electronic states were calculated through the plane-wave pseudopotential approach and generalized gradient approximation with Perdew–Burke–Ernzerhof functional (GGA-PBE).[25] The ultrasoft pseudopotentials were employed for all the atoms with a kinetic energy cutoff of 380 eV for the plane-wave basis. The Monkhorst–Pack meshes were ($6 \times 6 \times 3$), ($6 \times 10 \times 4$), and ($6 \times 6 \times 4$) for BiOCl ($2 \times 2 \times 2$), TiO_2 ($2 \times 1 \times 2$), and ZnO ($2 \times 2 \times 2$) supercells, respectively. The energy and force were converged to 10–5 eV per atom and 0.03 eV A^{-1}, respectively.

Supporting Information

Supporting Information is available from the Wiley Online Library or from the author.

Acknowledgements

This work was supported by National Natural Science Funds for Distinguished Young Scholars (21425728), National Basic Research Program of China (973 Program) (Grant No. 2013CB632402), National Science Foundation of China (Grant Nos. 21177048, 21377044, and 51472100), Key Project of Natural Science Foundation of Hubei Province (Grant No. 2013CFA114), and Self-Determined Research Funds of CCNU

from the Colleges' Basic Research and Operation of MOE (Grant No. CCNU14Z01001). We also thank the National Supercomputer Center in Jinan for providing high performance computation.

Received: November 25, 2014
Revised: February 3, 2015
Published online: February 26, 2015

[1] a) R. Asahi, T. Morikawa, T. Ohwaki, K. Aoki, Y. Taga, *Science* **2001**, *293*, 269; b) S. U. M. Khan, M. Al-Shahry, W. B. Ingler, *Science* **2002**, *297*, 2243; c) X. B. Chen, L. Liu, P. Y. Yu, S. S. Mao, *Science* **2011**, *331*, 746; d) J. Wang, D. N. Tafen, J. P. Lewis, Z. L. Hong, A. Manivannan, M. J. Zhi, M. Li, N. Q. Wu, *J. Am. Chem. Soc.* **2009**, *131*, 12290; e) C. Y. Yang, Z. Wang, T. Q. Lin, H. Yin, X. J. Lü, D. Y. Wan, T. Xu, C. Zheng, J. H. Lin, F. Q. Huang, X. M. Xie, M. H. Jiang, *J. Am. Chem. Soc.* **2013**, *135*, 17831.

[2] a) W. Choi, A. Termin, M. R. Hoffmann, *J. Phys. Chem.* **1994**, *98*, 13669; b) J. G. Tao, T. Luttrell, M. Batzill, *Nat. Chem.* **2011**, *3*, 296.

[3] G. Liu, L. Z. Wang, H. G. Yang, H. M. Cheng, G. Q. Lu, *J. Mater. Chem.* **2010**, *20*, 831.

[4] a) C. Burda, Y. B. Lou, X. B. Chen, A. C. S. Samia, J. Stout, J. L. Gole, *Nano Lett.* **2003**, *3*, 1049; b) G. Liu, L. Z. Wang, C. H. Sun, X. X. Yan, X. W. Wang, Z. G. Chen, S. C. Smith, H. M. Cheng, G. Q. Lu, *Chem. Mater.* **2009**, *21*, 1266; c) X. K. Li, N. Kikugawa, J. H. Ye, *Adv. Mater.* **2008**, *20*, 3816; d) B. Liu, H. M. Chen, C. Liu, S. C. Andrews, C. Hahn, P. D. Yang, *J. Am. Chem. Soc.* **2013**, *135*, 9995; e) J. Resasco, N. P. Dasgupta, J. R. Rosell, J. H. Guo, P. D. Yang, *J. Am. Chem. Soc.* **2014**, *136*, 10521; f) G. Liu, C. H. Sun, S. C. Smith, Z. G. Chen, G. Q. Lu, H. M. Cheng, *J. Am. Chem. Soc.* **2010**, *132*, 11642; g) Y. Wang, J. S. Zhang, X. C. Wang, M. Antonietti, H. R. Li, *Angew. Chem. Int. Ed.* **2010**, *49*, 3356; h) J. S. Zhang, M. W. Zhang, S. Lin, X. Z. Fu, X. C. Wang, *J. Catal.* **2014**, *310*, 24; i) K. Maeda, T. Takata, M. Hara, N. Saito, Y. Inoue, H. Kobayashi, K. Domen, *J. Am. Chem. Soc.* **2005**, *127*, 8286; j) J. Zhang, J. G. Yu, M. Jaroniec, J. R. Gong, **2012**, *12*, 4584; k) S. X. Ouyang, J. H. Ye, *J. Am. Chem. Soc.* **2011**, *133*, 7757.

[5] D. Chen, R. Viswanatha, G. L. Ong, R. G. Xie, M. Balasubramaninan, X. G. Peng, *J. Am. Chem. Soc.* **2009**, *131*, 9333.

[6] S. C. Erwin, L. J. Zu, M. I. Haftel, A. Efros, T. A. Kennedy, D. J. Norris, *Nature* **2005**, *436*, 91.

[7] a) X. B. Chen, C. Burda, *J. Am. Chem. Soc.* **2008**, *130*, 5018; b) C. D. Valentin, G. Pacchioni, A. Selloni, *Chem. Mater.* **2005**, *17*, 6656; c) J. G. Yu, G. P. Dai, Q. J. Xiang, M. Jaroniec, *J. Mater. Chem.* **2011**, *21*, 1049; d) S. W. Liu, C. Li, J. G. Yu, Q. J. Xiang, *CrystEngCom.* **2011**, *13*, 2533.

[8] a) H. G. Yang, C. H. Sun, S. Z. Qiao, J. Zou, G. Liu, S. C. Smith, H. M. Cheng, G. Q. Lu, *Nature* **2008**, *453*, 638; b) J. Pan, G. Liu, G. Q. Lu, H. M. Cheng, *Angew. Chem. Int. Ed.* **2011**, *50*, 2133; c) E. S. Jang, J. H. Won, S. J. Hwang, J. H. Choy, *Adv. Mater.* **2006**, *18*, 3309.

[9] a) J. Jiang, K. Zhao, X. Y. Xiao, L. Z. Zhang, *J. Am. Chem. Soc.* **2012**, *134*, 4473; b) K. Zhao, L. Z. Zhang, J. J. Wang, Q. X. Li, W. W. He, J. J. Yin, *J. Am. Chem. Soc.* **2013**, *135*, 15750 ; c) J. Li, Y. Yu, L. Z. Zhang, *Nanoscale* **2014**, *6*, 8473.

[10] J. H. Yu, B. Wei, L. Zhu, H. Gao, W. J. Sun, L. L. Xu, *Appl. Surf. Sci.* **2013**, *284*, 497.

[11] J. Li, L. Z. Zhang, Y. J. Li, Y. Yu, *Nanoscale* **2014**, *6*, 167.

[12] a) S. Ikeda, M. Hara, J. N. Kondo, K. Domen, H. Takahashi, T. Okubo, M. Kakihana, *Chem. Mater.* **1998**, *10*, 72; b) X. Wang, Q. Xu, M. R. Li, S. Shen, X. L. Wang, Y. C. Wang, Z. C. Feng, J. Y. Shi, H. X. Han, C. Li, *Angew. Chem. Int. Ed.* **2012**, *51*, 13089; c) H. Kato, A. Kudo, *J. Phys. Chem. B* **2001**, *105*, 4285.

[13] Q. Li, B. D. Guo, J. G. Yu, J. R. Ran, B. H. Zhang, H. J. Yan, J. R. Gong, *J. Am. Chem. Soc.* **2011**, *133*, 10878.

[14] a) G. Liu, J. Pan, L. C. Yin, J. T. Irvine, F. Li, J. Tan, P. Wormald, H. M. Cheng, *Adv. Funct. Mater.* **2012**, *22*, 3233; b) M. J. Kenney, M. Gong, Y. G. Li, J. Z. Wu, J. Feng, M. Lanza, H. J. Dai, *Science* **2013**, *342*, 836; c) A. Gasparotto, D. Barreca, D. Bekermann, A. Devi, R. A. Fischer, P. Fornasiero, V. Gombac, O. I. Lebedev, C. Maccato, T. Montini, G. V. Tendeloo, E. Tondello, *J. Am. Chem. Soc.* **2011**, *133*, 19362.

[15] a) L. Zhao, X. F. Chen, X. C. Wang, Y. J. Zhang, W. Wei, Y. H. Sun, M. Antonietti, M. M. Titirici, *Adv. Mater.* **2010**, *22*, 3317; b) F. Dong, H. Q. Wang, Z. B. Wu, *J. Phys. Chem. C* **2009**, *113*, 16717; c) X. Y. Wu, S. Yin, Q. Dong, C. S. Guo, T. Kimura, J. Matsushita, T. Sato, *J. Phys. Chem. C* **2013**, *117*, 8345.

[16] a) E. A. Reyes-Garcia, Y. P. Sun, K. R. Reyes-Gil, D. Raftery, *Solid State Nucl. Magn. Reson.* **2009**, *35*, 74; b) E. M. Rockafellow, X. W. Fang, B. G. Trewyn, K. Schmidt-Rohr, W. S. Jenks, *Chem. Mater.* **2009**, *21*, 1187.

[17] P. Pattabiraman, N. M. Rodriguez, B. Z. Jang, R. T. K. Baker, *Carbon* **1990**, *28*, 867.

[18] a) M. B. Dines, *J. Chem. Educ.* **1974**, *51*, 221; b) Y. Ebina, A. Tanaka, J. N. Kondo, K. Domen, *Chem. Mater.* **1996**, *8*, 2534; c) N. I. Kovtyukhova, Y. X. Wang, R. T. Lv, M. Terrones, V. H. Crespi, T. E. Mallouk, *J. Am. Chem. Soc.* **2013**, *135*, 8372.

[19] R. K. Nagarale, U. Hoss, A. Heller, *J. Am. Chem. Soc.* **2012**, *134*, 20783.

[20] J. E. D. Davies, *J. Inorg. Nucl. Chem.* **1973**, *35*, 1531.

[21] a) H. F. Cheng, B. B. Huang, Y. Dai, *Nanoscale* **2014**, *6*, 2009; b) Y. Y. Liu, W. J. Son, J. B. Lu, B. B. Huang, Y. Dai, M. H. Whangbo, *Chem. Eur. J.* **2011**, *17*, 9342; c) H. F. Cheng, B. B. Huang, Z. Y. Wang, X. Y. Qin, X. Y. Zhang, Y. Dai, *Chem. Eur. J.* **2011**, *17*, 8039; d) S. M. Sun, W. Z. Wang, *RSC Adv.* **2014**, *4*, 47136; e) L. Zhang, W. Z. Wang, S. M. Sun, Y. Y. Sun, E. P. Gao, J. Xu, *Appl. Catal. B* **2013**, *132*, 315; f) L. Zhang, W. Z. Wang, S. M. Sun, D. Jiang, E. P. Gao, *Appl. Catal. B* **2015**, *162*, 470; g) L. Q. Ye, Y. R. Su, X. L. Jin, H. Q. Xie, C. Zhang, *Environ. Sci.: Nano.* **2014**, *1*, 90; h) L. Q. Ye, L. Zan, L. H. Tian, T. Y. Peng, J. J. Zhang, *Chem. Commun.* **2011**, *47*, 6951; i) S. X. Weng, Z. X. Pei, Z. Y. Zheng, J. Hu, P. Liu, *ACS Appl. Mater. Interfaces.* **2013**, *5*, 12380; j) S. X. Weng, J. Hu, M. L. Lu, X. X. Ye, Z. X. Pei, M. L. Huang, L. Y. Xie, S. Lin, P. Liu, *Appl. Catal. B* **2015**, *163*, 205.

[22] X. M. Sun, Y. D. Li, *Angew. Chem. Int. Ed.* **2004**, *43*, 597.

[23] X. J. Lü, W. Yang, Z. W. Quan, T. Q. Lin, L. G. Bai, L. Wang, F. Q. Huang, Y. S. Zhao, *J. Am. Chem. Soc.* **2014**, *136*, 419.

[24] D. J. Norris, A. L. Efros, S. C. Erwin, *Science* **2008**, *319*, 1776.

[25] a) J. P. Perdew, K. Burke, M. Ernzerhof, *Phys. Rev. Lett.* **1996**, *77*, 3865; b) M. D. Segall, P. L. D. Lindan, M. J. Probert, C. J. Pickard, P. J. Hasnip, S. J. Clark, M. C. Payne, *J. Phys.: Condens. Matter* **2002**, *14*, 2717.